JOM
https://doi.org/10.1007/s11837-025-07634-2

TECHNICAL ARTICLE

Efficient and Green Recovery of Iron and Chromium from Laterite Residue Using Biochar

DONGYANG DOU,[1,2] BAOZHONG MA ,[1,2,3] ZHIHE CAO,[1,2,4] YONGQIANG CHEN,[1,2] and CHENGYAN WANG[1,2,5]

1.—State Key Laboratory of Advanced Metallurgy, University of Science and Technology Beijing, Beijing 100083, China. 2.—School of Metallurgical and Ecological Engineering, University of Science and Technology Beijing, 30 Xueyuan Road, Haidian District, Beijing 100083, China. 3.—e-mail: bzhma_ustb@yeah.net. 4.—e-mail: caozhihe1227@163.com. 5.—e-mail: chywang@yeah.net

Nickel, as a crucial metallic element, is extensively utilized in the new energy and stainless steel sectors. The rising demand for nickel in recent years has driven rapid progress in hydrometallurgical technology while also producing large amounts of laterite residue. At present, the laterite residue can be utilized to produce iron phosphate, representing a high-value utilization method. However, this approach is not effective for large-scale processing of the laterite residue. This research introduces a biomass-carbon-based smelting reduction ironmaking technology to efficiently handle the substantial amounts of laterite residue. Charcoal, as a biomass resource, is characterized by its high fixed carbon content and low ash content, making it an excellent reducing agent for the ironmaking process. Thermodynamic calculations were performed to analyze phase transformations, reaction mechanisms, and optimal conditions during metallization reduction. The optimal smelting reduction conditions were a mass ratio of charcoal to laterite residue of 0.21, 120 min, and 1475°C. Experimental results showed that under the optimal conditions, the product contained 95.76% iron and 2.64% chromium, with recovery of 95.09% for iron and 95.88% for chromium.

INTRODUCTION

The expanding electric vehicle industry and persistent stainless steel demand are jointly driving a significant increase in global nickel resource consumption. Laterite nickel ore is an important type of nickel resource, accounting for up to 70% of global nickel reserves, with iron content typically ranging between 25% and 50%.[1,2] As sulfide nickel ore reserves dwindle and nickel demand grows, the contribution share of laterite nickel ore to total nickel production has significantly increased.[3] In recent years, hydrometallurgical processes have advanced rapidly, with extensive application in nickel-cobalt extraction from limonitic laterite ores through three principal techniques: atmospheric acid leaching (AL),[4] high-pressure acid leaching (HPAL),[5] and nitric acid pressure leaching (NAPL).[6] During HPAL and NAPL hydrometallurgical processing, nickel dissolves into the leachate while iron and chromium report to the residue.[7] In HPAL, sulfur tends to remain in the leaching residue despite efficient nickel and cobalt extraction, greatly limiting its resource recovery potential.[8] The residue from NAPL after nickel and cobalt extraction contains up to 60% iron and is completely sulfur-free.[9] Currently, NAPL residue is predominantly disposed of through either landfilling or deep-sea deposition. This practice causes the loss of valuable metals such as iron and chromium and poses persistent environmental risks to terrestrial and marine ecosystems.[10] Research indicates that the residue from NAPL can be processed to prepare iron phosphate products.[3] While this approach achieves high-value utilization of the leaching residue, it does not constitute an effective solution for large-

(Received May 7, 2025; accepted July 9, 2025)

Published online: 07 August 2025

scale treatment of such industrial by-products. The NAPL laterite residue contains high concentrations of iron (60.0 wt.%) and chromium (2.0 wt.%), making it a potential raw material for extracting these two strategic metals.[11] NAPL residue is sulfur-free and contains high iron content (up to 60%), primarily in the form of hematite,[12] making it an excellent raw material for iron smelting. In 2022, China imported 1107 million tons of iron ore to balance domestic supply and demand, demonstrating a critically high external dependence level of 90% in its iron ore supply chain.[13] Consequently, using NAPL residue as an alternative iron source for ironmaking could simultaneously resolve residue accumulation problems and mitigate iron ore supply shortages.

The steel industry faces three major challenges—resource scarcity, energy limits, and environmental compliance—while still using polluting, energy-intensive production methods.[14] Biomass, as a renewable energy source, exhibits distinct advantages over conventional fuels or reducing agents, including carbon neutrality, cost-effectiveness, low sulfur content, and superior reducing capabilities.[15,16] Woody biomass, characterized by its wide availability, low ash content, and relatively high fixed carbon content, emerges as an ideal feedstock for biomass utilization.[17,18] Despite its advantages, woody biomass requires preprocessing for efficient utilization due to low bulk density and high transport costs.[19]

Charcoal is a carbon-rich solid product obtained from the pyrolysis of woody biomass under oxygen-deprived or anaerobic conditions.[20] Compared to raw woody biomass, it exhibits superior properties including higher fixed carbon content and greater bulk density.[21] Ooi et al. conducted sintering experiments using charcoal as fuel and found that a 20% proportion of charcoal could provide the same amount of thermal energy as coke fines.[22] Macphee et al. experimentally produced industrial-grade coke by adding up to 10% charcoal to the coking coal blend and found that the incorporation of charcoal effectively reduced CO_2 emissions.[23] Wang et al. developed a static heat and mass balance model to investigate the substitution rates of charcoal, pyrolyzed materials, and wood pellets for pulverized coal injection in blast furnaces.[24] The results demonstrated that 166.7 kg/tHM of charcoal could effectively replace 155 kg/tHM of pulverized coal. The study by Fan et al. explored charcoal's potential as an alternative to coke powder in sample production across various replacement levels.[25] When 40% of coke was replaced with charcoal, the sample's porosity and FeO content both increased. This led to an improvement in the reduction rate index from 79.8% to 84.3%, resulting in effective enhancement of the reduction performance.

This study innovatively develops a green, low-carbon technology for laterite residue valorization, achieving the efficient recovery of strategic metals (Fe, Cr) while simultaneously addressing the dual challenges of laterite residue accumulation and iron ore resource scarcity. This study investigated the reduction behavior of iron-bearing minerals using charcoal as a reducing agent, with particular focus on phase transformation mechanisms during metallization. The effects of different processing conditions on the recovery efficiency and content of iron and chromium were systematically examined. The research aims to greenly valorize laterite residue, ease ironmaking raw material shortages, and support carbon peak and neutrality goals.

EXPERIMENT

Experimental Materials

The biomass feedstock used in this study was wood chips sourced from Sichuan Province, China. As shown in Table I, the proximate analysis of the wood chips revealed a relatively low fixed carbon content of 16.74% and a high volatile matter content of 73.69%. To determine the pyrolysis temperature range for wood chip conversion to charcoal, the thermal stability of wood chips was analyzed using simultaneous thermal analysis (STA 449 F5, Germany) under nitrogen atmosphere. The resulting thermogravimetric-differential scanning calorimetry (TG-DTG) curves are shown in Fig. 1a. The thermogravimetric (TG) curve of wood chips was directly measured using the simultaneous thermal analyzer, and the derivative thermogravimetric (DTG) curve was derived from the TG data. When the pyrolysis temperature was < 135°C, a significant decrease was observed in the TG curve, primarily attributed to the removal of bound water from the wood chips. At precisely 135°C, the wood chips exhibited a mass loss of 4.70%. A sharp decline in both TG and DTG curves occurred within the temperature range of 230–328°C, mainly resulting from substantial decomposition of volatile components. Upon reaching 800°C, the cumulative mass loss reached $-$ 74.89%. When the temperature surpassed 800°C, stabilization of both TG and DTG curves was observed, demonstrating complete volatile matter pyrolysis and successful charcoal formation.

NAPL laterite residue used in this experiment was sourced from a hydrometallurgical nickel processing enterprise in Sichuan Province, China. The concentrations of Fe, Cr, Si, Mg, and Al in the NAPL residue were determined by ICP-OES, with the elemental composition presented in Table II. The results showed the NAPL residue contained 59.62% Fe and 1.63% Cr. Mineralogical analysis by XRD (Fig. 1b) demonstrated that iron primarily existed as hematite and chromite. Although the SiO_2 content was 5.16 wt.%, no crystalline silicon-bearing phases were detected in the XRD pattern. As shown in Fig. 2 the NAPL residue particles exhibited uniform spherical morphology with diameters ranging from 0.3 μm to 1 μm. These findings

Table I. Industrial analysis results of wood chips(wt.%)

Component	Fixed C	Ash	Volatile matter	Moisture
Content	16.74	0.45	73.69	9.12

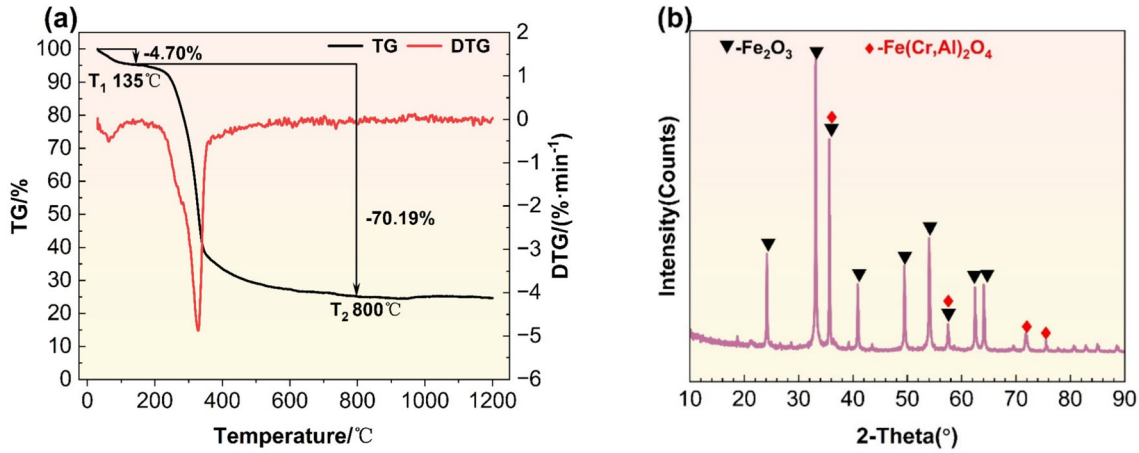

Fig. 1. Characterization of raw materials: (a) thermogravimetric analysis of wood chips; (b) XRD pattern of laterite residue.

Table II. Compositions of laterite residue (wt.%)

Composition	Fe	Al	Cr	Si	Mg
Content	59.62	0.37	1.63	2.41	0.15

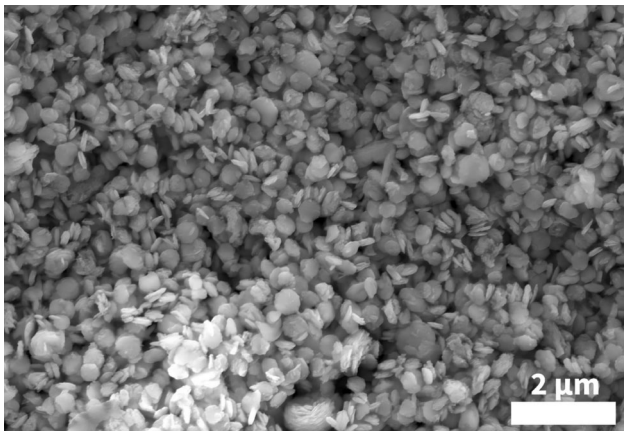

Fig. 2. SEM image of laterite residue.

demonstrate that the NAPL residue—characterized by high iron content, simple phase composition, and fine particle size—represents a high-quality raw material for ironmaking.

Experimental Method

The wood chips were carbonized in a tube furnace at 800°C for 30 min under nitrogen atmosphere, followed by cooling and crushing to produce charcoal, with its industrial analysis results shown in Table III. Both charcoal and NAPL residue were ground to 200 mesh and thoroughly mixed at predetermined mass ratios. The thoroughly mixed material was then transferred into a corundum crucible. The reduction experiments were conducted in a tube furnace under a nitrogen atmosphere with a heating rate of 5°C/min. During the reduction process, a N_2 gas flow rate of 0.3 L/min was maintained. Then, the products were cooled to 25°C in the tube furnace, with detailed experimental parameters provided in Table IV.

RESULTS AND DISCUSSION

Thermodynamic Analysis

As shown in Tables I and III, the volatile matter content of wood chips decreased significantly after carbonization treatment, dropping from 73.69% to 11.88%, while the fixed carbon content increased substantially, rising from 16.74% to 82.81%.

As shown in Fig. 1b, the primary iron-bearing minerals in the NAPL residue are hematite and chromite. The potential chemical reactions that may occur during the reduction process are presented in Table V. The ΔG^{θ} values for these reactions (within the temperature range of 500–1600°C) were calculated using the reaction module of FactSage 8.3, with the computational results presented in Fig. 3a and b.

As shown in Fig. 3a, when the temperature exceeds 1253°C, the ΔG^{θ} values for reactions (1, 2) become negative, demonstrating that both chromite

Table III. Industrial analysis results of charcoal (wt.%)

Component	Fixed C	Moisture	Ash	Volatile matter
Content	82.81	1.59	4.32	11.88

Table IV. Parameters of the reduction experiments

Condition	Fixed paraments	Values
Biochar/laterite residue (g/g)	1500°C, 180 min	0.19, 0.21, 0.23, 0.25
Temperature/°C	0.21, 180 min	1450, 1475, 1500, 1525
Reduction time/min	0.21, 1475°C	60, 90, 120, 150, 180

Table V. Chemical reactions of reduction

No.	Reaction equation
1	$FeCr_2O_4 + C = Fe + Cr_2O_3 + CO$
2	$Cr_2O_3 + 3C = 2Cr + 3CO$
3	$Fe_2SiO_4 + 2C = 2Fe + SiO_2 + 2CO$
4	$FeCr_2O_4 + CO = Fe + Cr_2O_3 + CO_2$
5	$Cr_2O_3 + 3CO = 2Cr + 3CO_2$
6	$Fe_2SiO_4 + 2CO = 2Fe + SiO_2 + 2CO_2$
7	$CO_2 + C = 2CO$
8	$3Fe_2O_3 + C = 2Fe_3O_4 + CO$
9	$Fe_3O_4 + C = 3FeO + CO$
10	$FeO + C = Fe + CO$
11	$3Fe_2O_3 + CO = 2Fe_3O_4 + CO_2$
12	$Fe_3O_4 + CO = 3FeO + CO_2$
13	$FeO + CO = Fe + CO_2$
14	$2FeO + SiO_2 = Fe_2SiO_4$

and chromium oxide can be effectively reduced by C, leading to metallic Cr formation. When the temperature exceeds 800°C, reaction (3) becomes thermodynamically favorable, enabling the reduction of Fe_2SiO_4 by carbon to produce metallic Fe and SiO_2. Based on the ΔG^{θ} values of reactions (4–6), the reduction of Cr_2O_3, $FeCr_2O_4$, and Fe_2SiO_4 by CO is thermodynamically unfavorable. At temperatures exceeding 702°C, reaction (7) becomes thermodynamically favorable. As shown in Fig. 3b, the ΔG^{θ} values of reactions (8–10) decrease progressively with increasing temperature. At temperatures > 725°C, the ΔG^{θ} values for reactions (8–10) all become negative. Thermodynamically, this confirms that hematite can be reduced by C to form metallic Fe. Based on reactions (11, 12), when the temperature is > 538°C, Fe_2O_3 can be sequentially reduced by CO to Fe_3O_4 and then to FeO. When the temperature is < 560°C, FeO can be reduced by CO to metallic Fe. However, as the temperature increases, reaction (13) becomes thermodynamically unfavorable. When the temperature exceeds 702°C, reaction (7) becomes feasible, leading to a gradual increase in CO concentration. As illustrated in Fig. 3c, the ΔG value of reaction (13) becomes negative when the P_{CO}/P_{CO2} ratio increases. Consequently, an increase in the P_{CO}/P_{CO2} ratio promotes the occurrence of reaction (13). For reaction (14), SiO_2 reacts with iron oxides to form fayalite. However, with increasing temperature, the ΔG^{θ} for reaction (14) shows a progressive increase. Therefore, moderate temperature elevation can effectively suppress the spontaneous progression of reaction (14).

The equilibrium composition of final products was calculated using the Equilib module in FactSage 8.3, incorporating the "FSstel," "FactPS," and "FToxid" databases. Components with concentrations $< 10^{-5}$ were considered negligible and excluded from the results. In this simulation module, the initial mass of NAPL residue was set as 100 g, with the initial masses of additional input materials provided in Table VI.

Figure 3e demonstrates that the spinel phase, composed predominantly of Fe_3O_4 and chromite, remains stable without decomposition below 650°C. As shown in Fig. 3e and f, the Fe_3O_4 phase nearly vanishes at 700°C, consistent with the $\Delta G^{\theta} - T$ relationship of reaction (9). As shown in Fig. 3d and e, the chromite phase demonstrates remarkable stability until 1000°C, where it completely decomposes with concomitant formation of Cr_2O_3. At 1100°C, the mass of $Cr_{(s)}$ attains its maximum value of 1.464 g, coinciding with the complete disappearance of Cr_2O_3. The formation temperature of Cr is lower than the theoretical temperature predicted by reaction (2), likely because of the catalytic effect of metallic iron on chromium reduction.[26] Within the 650–1350°C temperature range, metallic iron-containing phases including both BCC and FCC structures are formed. When the temperature exceeds 650°C, iron carbides begin to generate, reaching their maximum mass (7.3996 g) at 1100°C. These carbides completely decompose by 1400°C. At 800°C, $Fe_{(s)}$ reaches its maximum mass of 56.297 g. $Fe_{(liquid)}$ formation initiates at 1150°C. As the temperature increases, the mass of $Fe_{(s)}$ and $Cr_{(s)}$ progressively decreases, while that of $Fe_{(l)}$ and $Cr_{(l)}$ correspondingly increases. At 1400°C, both $Fe_{(l)}$ and $Cr_{(l)}$ attain their respective maximum masses of

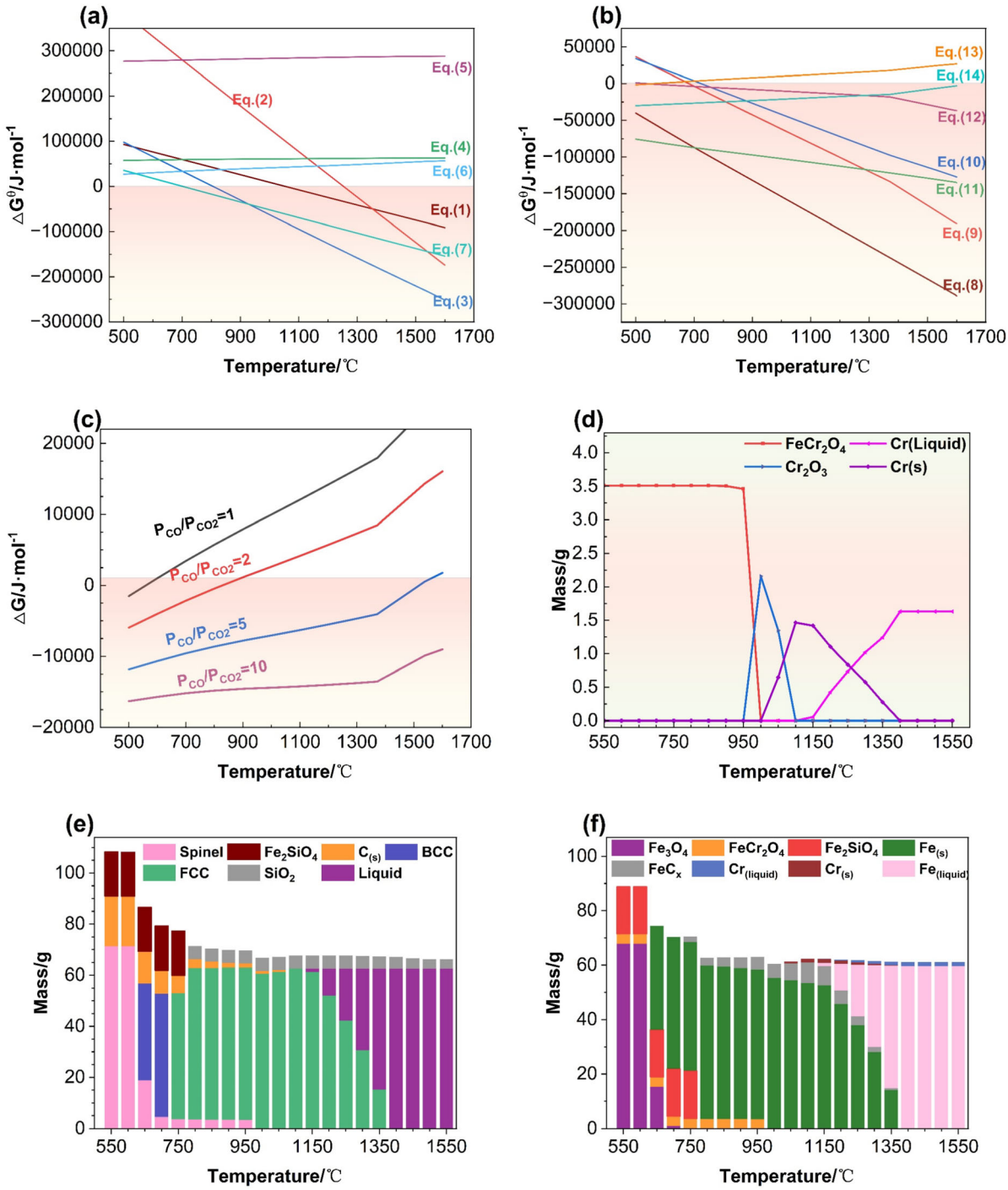

Fig. 3. Thermodynamic analysis of the reduction process: (a, b) $\triangle G^{\theta} - T$ relation for the equations at 500–1600°C; (c) $\triangle G - T$ relation for the CO-FeO reaction under different P_{CO}/P_{CO2}; (d) mass of Cr-bearing mineral phases; (e) mass of stable mineral phases; (f) mass of Fe-bearing mineral phases.

Table VI. Initial mass of input components in the thermodynamic calculation

Component	Hematite	Quartz	Chromite	C
Content/g	83.91	5.16	3.51	21

59.564 g and 1.63 g. When the temperature exceeds 800°C, the Fe_2SiO_4 phase completely disappears, and the SiO_2 phase begins to form, corresponding to the $\Delta G^{\theta} - T$ relationship in reaction (14). Additionally, based on the principle of gravitational settling, the liquid metal phase will settle to the bottom of the crucible, while the SiO_2 phase will float above the metal phase. This separation of slag and metal

phases facilitates the recovery of iron and chromium.

Therefore, the most suitable theoretical temperature for molten reduction should be > 1400°C. The molten reduction process operates at 1500°C, selected to provide a sufficient margin above the minimum required temperature for efficient and complete reduction reactions.

Experiments of Molten Metallization Reduction

This study investigates the effects of temperature, the mass ratio of charcoal to laterite residue, and reaction time on molten reduction. The experimental conditions are shown in Table IV.

Effect of the Mass Ratio of Charcoal to Laterite Residue

As shown in Fig. 4, the mass ratio of charcoal to laterite residue has a relatively minor effect on the iron content, with values ranging between 91.60% and 95.16%. However, this ratio significantly impacts both chromium content and recovery. When the mass ratio is 0.19, the Cr content is only 1.28%, whereas it increases to 2.47% when the ratio rises to 0.21. According to reactions (1, 2, 4, 5), chromite and Cr_2O_3 are easily reduced by C but not so readily by CO. At a mass ratio of 0.19, the C in the charcoal is insufficient to reduce most of the Cr_2O_3. Therefore, the recovery of chromium remains quite low.

When the mass ratio surpasses 0.21, a gradual decline in iron recovery becomes evident. This is mainly because the increased mass ratio leads to a higher content of residual C in the slag, which in turn raises the viscosity of the slag. This affects the separation of slag and iron, causing iron to be incorporated into the slag. At a mass ratio of 0.21, the recovery of iron and chromium is optimized, with recovery reaching 97.12% and 92.20%, respectively. Therefore, the selected mass ratio is 0.21.

Effect of Temperature

The effects of temperature on the iron and chromium content in the products and the recovery are shown in Fig. 5. As seen in Fig. 5a, both the content and recovery of iron and chromium initially increase with temperature and then tend to level off. When the temperature rises from 1450°C to 1475°C, the iron content increases from 89.20% to 94.86%, and the chromium content rises from 2.25% to 2.51%. Meanwhile, the recovery of iron increases from 87.12% to 93.84% and that of chromium rises from 80.38% to 90.81%. The increase in iron and chromium content and recovery is primarily attributed to elevated temperature, which reduces slag viscosity and enhances slag-metal separation. When the temperature continues to rise, the lack of significant changes in the content and recovery of iron and chromium may be attributed to the complete melting of the slag.

Effect of Time

The effects of reduction time on content of iron and chromium are shown in Fig. 6a, while their recovery is shown in Fig. 6b. As shown in Fig. 6a, when the reduction time is 120 min, the iron content reaches its peak at 95.76%. As reduction time increases, chromium content fluctuates slightly between 2.21% and 2.64%. As shown in Fig. 6b, when the reduction time is 120 min, the recovery of both iron and chromium are relatively high, with iron recovery at 95.09% and chromium recovery at 95.88%. Therefore, the optimal reduction time is determined to be 120 min.

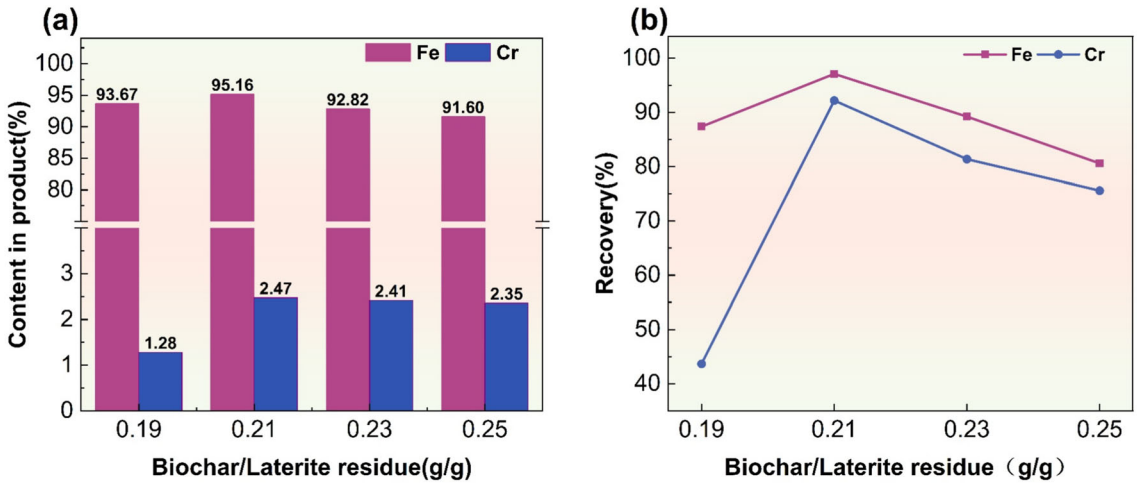

Fig. 4. The effect of the mass ratio of charcoal to laterite residue on (a) the iron and chromium content in the products and (b) the recovery of iron and chromium.

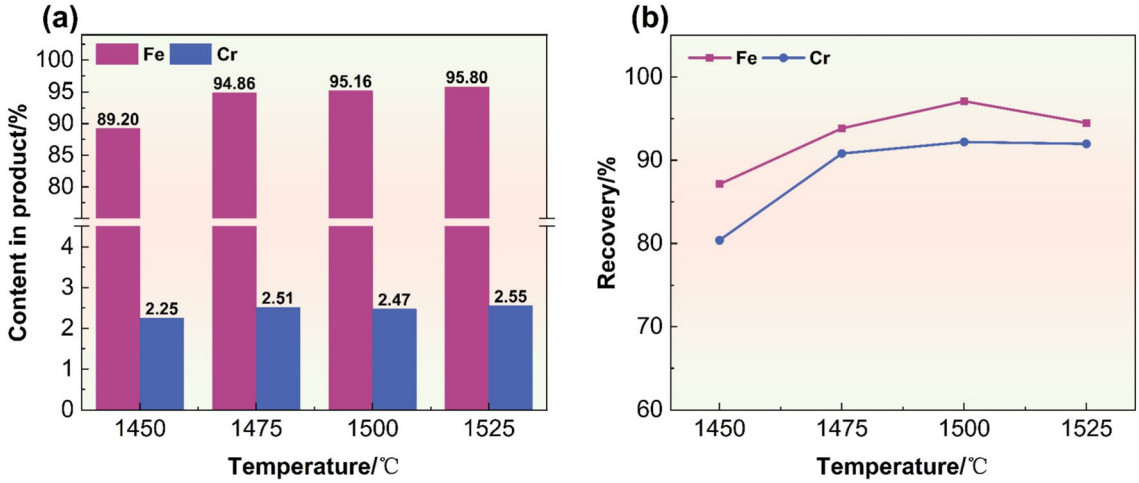

Fig. 5. The effect of temperature on (a) the iron and chromium content in the products and (b) the recovery of iron and chromium.

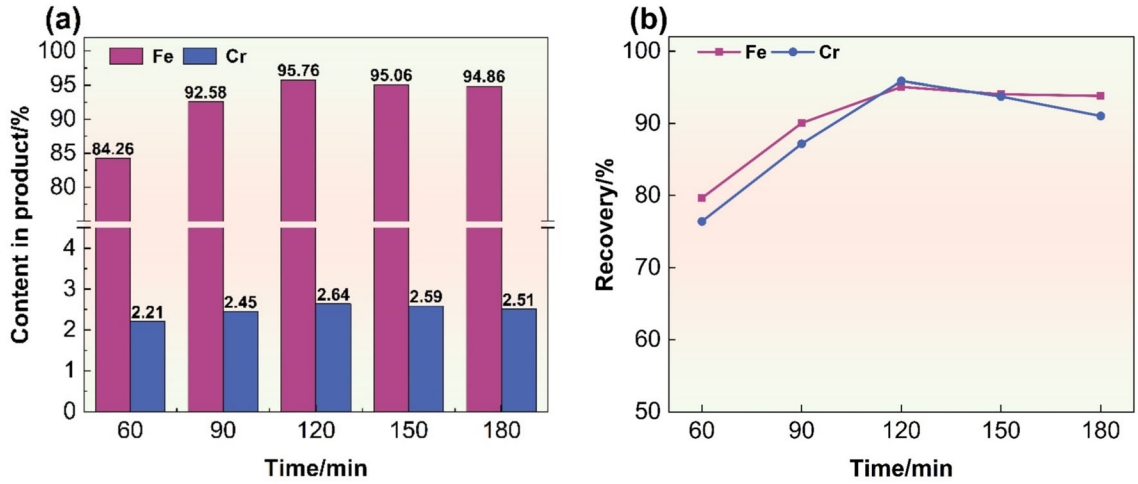

Fig. 6. The effects of reduction time on (a) the iron and chromium content in product and (b) the recovery of iron and chromium.

Therefore, the optimal conditions for the smelting reduction of laterite residue using charcoal are as follows: a reaction temperature of 1475°C, a mass ratio of charcoal to laterite residue of 0.21, and a reduction time of 120 min. Under these conditions, the product contains 95.76% iron and 2.64% chromium. Moreover, the recovery of iron and chromium is 95.09% and 95.88%, respectively.

When the reaction conditions are 1475°C, a mass ratio of 0.21, and 120 min, the XRD patterns of the product and slag are as shown in Fig. 7. As evidenced by the XRD pattern in Fig. 7a, only sharp iron diffraction peaks are observed under these conditions, revealing iron as the dominant component. As Fig. 7b shows, the unreduced Fe_2O_3 and $FeCr_2O_4$ entered the slag phase. SiO_2, MgO, and magnesium aluminosilicates, among other impurities, have also entered the slag phase. In addition, the reduced FeO and a small amount of metallic iron have also entered the slag. Figure 7c and d shows the product images under optimal conditions, demonstrating effective slag-metal separation with slag distributed in the upper layer above the metallic phase.

Phase Transformations and Microstructural Evolutions

As shown in Fig. 8, when the temperature is 1450°C, the product not only shows the characteristic peaks of iron but also exhibits the characteristic peaks of aluminosilicates. However, when the temperature increases to 1475°C, the XRD pattern of the product exhibits exclusively the characteristic diffraction peaks of metallic iron, with complete absence of any impurity phases. Moreover, with the increase in temperature, the intensity of the iron characteristic peaks also gradually increases. This is because as the temperature increases, the viscosity of the slag decreases, which promotes the reduction of iron and the separation of slag and

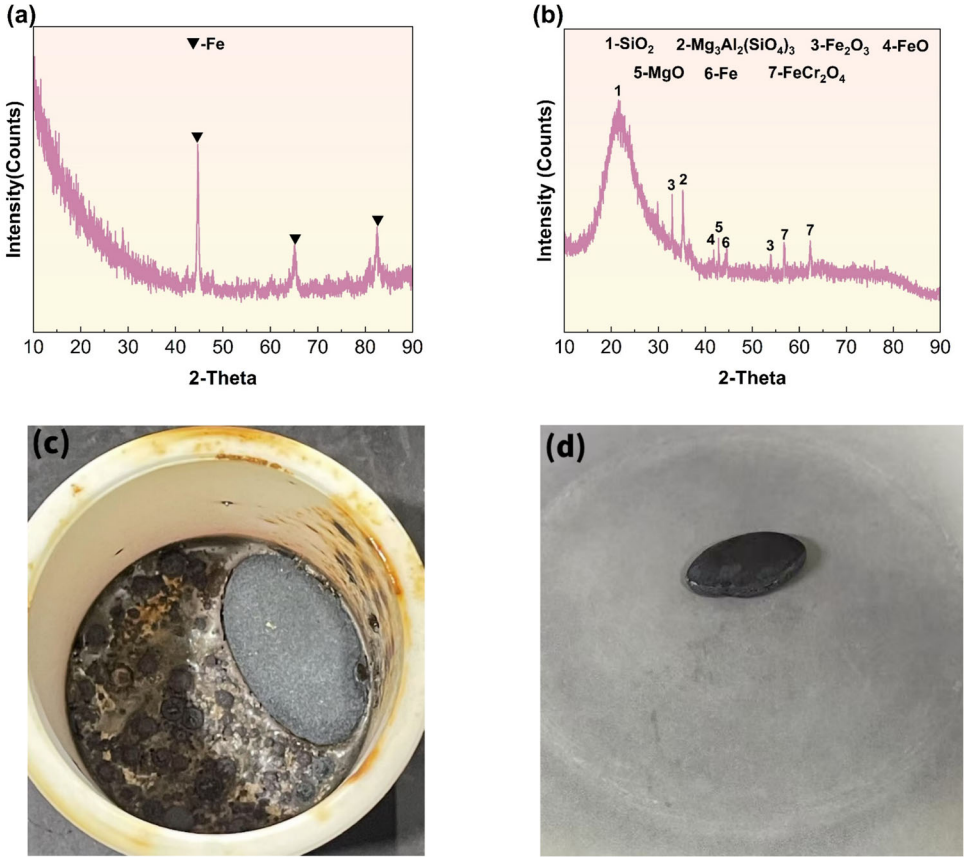

Fig. 7. (a) XRD pattern of the product; (b) XRD pattern of the slag; (c, d) product images obtained at 1475°C with a mass ratio of 0.21 and reduction time of 120 min.

metal. As Fig. 8b shows, the slag contains unreduced Fe_2O_3 and $FeCr_2O_4$, the intermediate product FeO, and the reduced metallic iron. Moreover, with the increase in temperature, the characteristic peak intensities of Fe, $FeCr_2O_4$, and Fe_2O_3 in the slag all decrease. This phenomenon primarily occurs because moderate temperature elevation facilitates the reduction of iron-bearing minerals while improving slag-metal separation efficiency, consequently minimizing iron and chromium losses.

Figure 8c and d illustrates the XPS characteristics of Fe $2p_{3/2}$ and Cr $2p_{3/2}$ for the product under different temperature conditions. According to the literature,[27] the binding energy of Fe $2p_{3/2}$ for metallic iron is 706.7 eV. As shown in Fig. 8c, in the product obtained at 1450°C, the fitted peaks of Fe $2p_{3/2}$ at 706.60 eV are indicative of metallic iron. Meanwhile, in the product obtained at 1475°C, the fitted peak of Fe $2p_{3/2}$ at 706.97 eV also corresponds to metallic iron.

In the literature,[28] the binding energies of Cr $2p_{3/2}$ for Cr_2O_3 and metallic chromium are 576.8 eV and 574.3 eV, respectively. In Fig. 8d, the fitted peaks of Cr $2p_{3/2}$ in the product at 1450°C, located at 574.08 eV and 576.61 eV, correspond to Cr_2O_3 and metallic chromium, respectively. At this temperature, Cr_2O_3 is generated from the reduction of $FeCr_2O_4$, but it is not fully converted to metallic chromium. In the product obtained at 1475°C, the fitted peak of Cr $2p_{3/2}$ at 574.16 eV corresponds to metallic chromium. Therefore, it can be concluded that appropriately increasing the temperature plays a crucial role in promoting the deep reduction of both iron and chromium. This improved reduction process enables a more thorough separation of slag and iron, ultimately leading to a more efficient recovery of iron and chromium. The results highlight the importance of optimizing the reaction temperature to achieve improved separation and recovery of valuable metals during the process.

In Fig. 9, the detailed microstructure and element distribution of the product under the conditions of 1475°C, a mass ratio of 0.21, and 120 min are clearly presented. As shown in Fig. 9, the product is predominantly composed of Fe and Cr elements, with both Cr and Fe exhibiting a highly uniform distribution throughout the material. Additionally, the absence of significant distribution of impurity elements like Si and O suggests that the product has a highly pure elemental composition. At a specific point designated as point 1, the content of Fe, Cr, and C was precisely measured to be 92.14%, 2.63%, and 5.23%, respectively. In conjunction with Fig. 7, which offers supplementary information, it

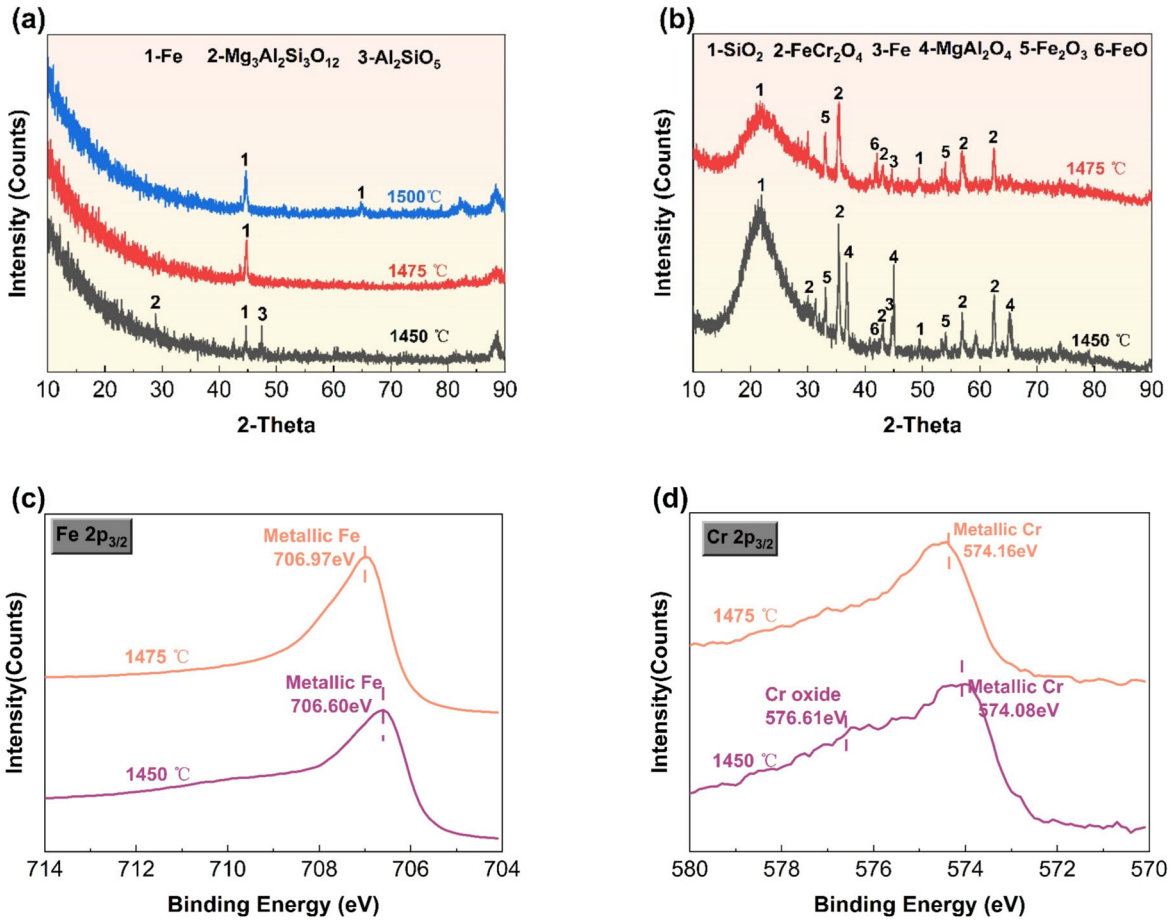

Fig. 8. Characterization analysis at different temperatures: (a) XRD of product; (b) XRD of slag; (c) Fe $2p_{3/2}$ of product; (d) Cr $2p_{3/2}$ of product.

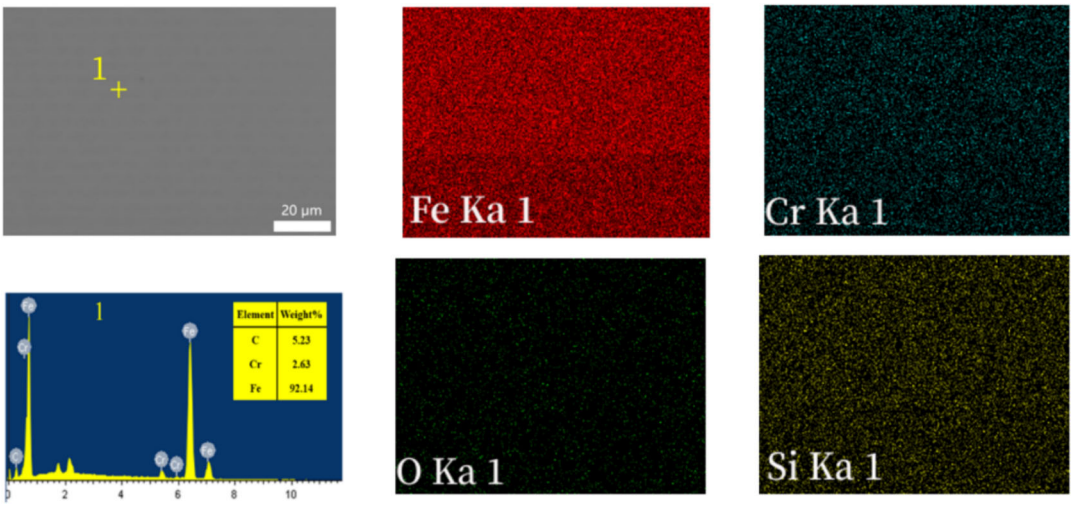

Fig. 9. The EDS/SEM analysis of the product under the conditions of 1475°C, a mass ratio of 0.21, and 120 min.

can be further confirmed that the product is primarily composed of metallic iron, with a notable presence of metallic chromium.

Based on the experimental results and thermodynamic analysis, the metallization reduction process of iron-bearing minerals and chromium-bearing minerals is illustrated in Fig. 10. The

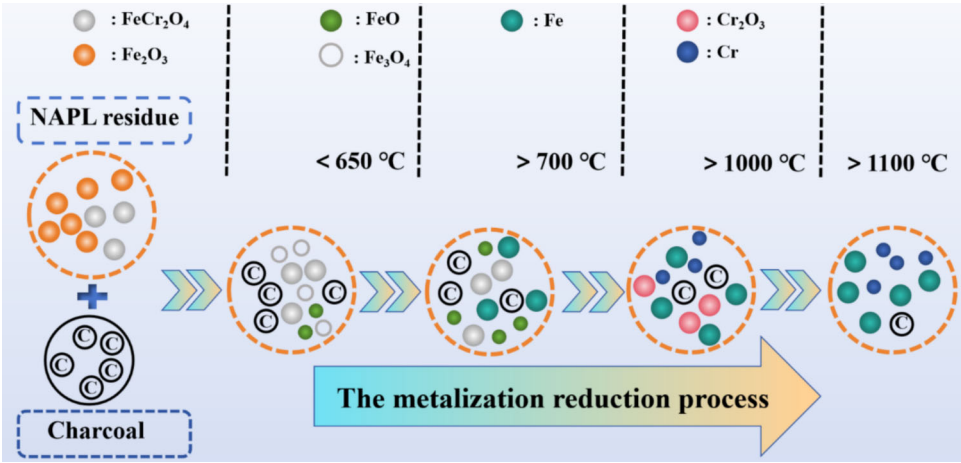

Fig. 10. The metallization reduction process of iron- and chromium-bearing minerals.

reduction sequence of chromite is: $FeCr_2O_4 \rightarrow Cr_2O_3 \rightarrow Cr$. The reduction sequence of hematite is: $Fe_2O_3 \rightarrow Fe_3O_4 \rightarrow FeO \rightarrow Fe$.

Economic Analysis and Sustainability Analysis

Comparative parameters of charcoal and coke reductants (supplementary Table S-I), along with economic cost analysis (supplementary formulas (1)–(3)) and sustainability assessment of charcoal (supplementary formulas (4)–(5)), are detailed in the Supplementary Material (refer to online supplementary material). The use of charcoal as a reducing agent in hot metal production offers dual advantages: it requires lower production costs compared to conventional coke-based processes while effectively reducing carbon dioxide emissions. China's abundant forest biomass resources, coupled with their renewable characteristics, provide sustainable feedstock security for green iron ore reduction processes. Therefore, charcoal demonstrates outstanding advantages in terms of economic viability and sustainability, making it an ideal alternative to traditional reducing agents in ironmaking processes.

CONCLUSION

This paper investigates the process of molten reduction of laterite residues using biomass char (charcoal). Thermogravimetric analysis was conducted on the wood chips to determine their optimal pyrolysis temperature. Through experimental operations and various characterization techniques, the reduction process, agglomeration behavior of iron and chromium, and migration and distribution patterns of certain impurity elements were thoroughly analyzed. Moreover, the process parameters were optimized experimentally to identify the optimal process conditions.

After pyrolysis treatment, the fixed carbon content in the charcoal produced from wood chips significantly increased from 16.74% to 82.81%, while the volatile matter content decreased from 73.69% to 11.88%. The laterite residue contains 59.62% iron, primarily as hematite, and 1.63% chromium, mainly as chromite. Its microparticles are uniformly round with diameters ranging from 0.3 μm to 1 μm.

In molten reduction, the reduction sequences of hematite and chromite are $Fe_2O_3 \rightarrow Fe_3O_4 \rightarrow FeO \rightarrow Fe$ and $FeCr_2O_4 \rightarrow Cr_2O_3 \rightarrow Cr$, respectively. The increase in temperature and the mass ratio of charcoal to laterite residue significantly enhanced the recovery of iron and chromium. Experiments showed that a reaction temperature of 1475°C, a mass ratio of charcoal to laterite residue of 0.21, and a reduction time of 120 min are the optimal conditions. Under these conditions, the content of iron and chromium in the product reached 95.76% and 2.64%. Meanwhile, the recovery of iron and chromium in the product was 95.09% and 95.88%, respectively. Moreover, charcoal-based ironmaking has economic cost advantages in resource-rich areas and excels in sustainability because of its use of renewable resources, reduced dependence on fossil fuels, and significant carbon emission reduction benefits.

SUPPLEMENTARY INFORMATION

The online version contains supplementary material available at https://doi.org/10.1007/s11837-025-07634-2.

ACKNOWLEDGMENTS

This work was supported by the National Natural Science Foundation of China (U2202254) and the

National Key Research and Development Program of China (2021YFC2902501).

COMPETING INTERESTS

On behalf of all authors, the corresponding author states that there is no conflict of interest.

REFERENCES

1. L. Mweene, G. Allan, J. Hee-Eun, I. Sadia, and H. Kim, *Miner. Process. Extract. Metall. Rev.* 45, 539 https://doi.org/10.1080/08827508.2023.2214668 (2024).
2. S. Cao, L. Chang, X. Bi, S. Luo, and J. Liu, *Min. Metall. Explor.* 39, 129 https://doi.org/10.1007/s42461-021-00518-4 (2022).
3. Z. Cao, B. Ma, Q. Jing, P. Xing, B. Liu, and C. Wang, *Ceram. Int.* 46, 11304 https://doi.org/10.1016/j.ceramint.2020.01.159 (2020).
4. G. Prameswara, I. Amin, A. Ulfah, I. Trisnawati, H. Petrus, and F. Puspita, *Mining Metall. Explor.* 41, 1025 https://doi.org/10.1007/s42461-024-00947-x (2024).
5. P. Zhang, L. Sun, H. Wang, J. Cui, and J. Hao, *J. Clean. Prod.* 228, 1 https://doi.org/10.1016/j.jclepro.2019.04.305 (2019).
6. W. Zhang, B. Ma, C. Wang, and Y. Chen, *Sep. Purif. Technol.* 350, 127780 https://doi.org/10.1016/j.seppur.2024.127780 (2024).
7. V. Ponomar, J. Yliniemi, E. Adesanya, K. Ohenoja, and M. Illikainen, *J. Clean. Prod.* 330, 129900 (2022).
8. E. Stamboliadis, G. Alevizos, and J. Zafiratos, *Miner. Eng.* 17, 245 https://doi.org/10.1016/j.mineng.2003.08.015 (2004).
9. Z. Cao, B. Ma, C. Wang, Y. Chen, B. Liu, P. Xing, and W. Zhang, *Miner. Eng.* 152, 106365 (2020).
10. L. Gao, Z. Liu, Y. Pan, Y. Ge, C. Feng, M. Chu, and J. Tang, *Min. Metall. Explor.* 36, 375 https://doi.org/10.1007/s42461-018-0012-z (2019).
11. B. Ma, C. Wang, W. Yang, F. Yin, and Y. Chen, *Miner. Eng.* 50–51, 106 https://doi.org/10.1016/j.mineng.2013.06.014 (2013).
12. Z. Cao, B. Ma, J. Zhou, Y. Chen, and C. Wang, *Process. Saf. Environ. Prot.* 168, 1 https://doi.org/10.1016/j.psep.2022.09.053 (2022).
13. P. Tae-Woo Lee, Z. Song, P. Chhetri, and S. Shin, *Ocean Coast. Manag.* 260, 107483 https://doi.org/10.1016/j.ocecoaman.2024.107483 (2025).
14. R. Wei, K. Meng, H. Long, and C. Xu, *Renew. Sustain. Energy Rev.* 199, 114475 (2024).
15. A. Setiawan, M. Rhamdhani, M. Pownceby, N. Webster, and S. Harjanto, *J. Sustain. Metall.* 7, 1819 https://doi.org/10.1007/s40831-021-00457-w (2021).
16. M. Sommerfeld and B. Friedrich, in: REWAS 2022: Developing Tomorrow's Technical Cycles (Volume I), ed. A. Lazou, K. Daehn, C. Fleuriault, M. Gökelma, E. Olivetti and C. Meskers (Springer International Publishing: Cham, 2022), pp 607–619.
17. S. Vassilev, D. Baxter, L. Andersen, and C.G. Vassileva, *Fuel* 89, 913 (2010).
18. H. Suopajärvi, K. Umeki, and E. Mousa, *Appl. Energy* 213, 384 (2018).
19. D. Khasraw, C. Martin, J. Herbert, and Z. Li, *Fuel* 368, 131459 (2024).
20. M. Antal, and M. Grønli, *Ind. Eng. Chem. Res.* 42, 1619 https://doi.org/10.1021/ie0207919 (2003).
21. A. Datta, A. Hossain, and S. Roy, *Asian J. Chem.* https://doi.org/10.14233/ajchem.2019.22098 (2019).
22. T. Ooi, E. Aries, B. Ewan, D. Thompson, D. Anderson, R. Fisher, T. Fray, and D. Tognarelli, *Miner. Eng.* 21, 167 (2008).
23. J. MacPhee, J. Gransden, L. Giroux, and J. Price, *Fuel Process. Technol.* 90, 16 https://doi.org/10.1016/j.fuproc.2008.07.007 (2009).
24. C. Wang, M. Larsson, J. Lövgren, L. Nilsson, P. Mellin, W. Yang, H. Salman, and A. Hultgren, *Energy Procedia* 61, 2184 https://doi.org/10.1016/j.egypro.2014.12.105 (2014).
25. X. Fan, Z. Ji, M. Gan, X. Chen, Q. Li, and T. Jiang, *Ironmak. Steelmak.* 43, 5 https://doi.org/10.1179/1743281215Y.0000000040 (2016).
26. Y. Zhang, Y. Liu, and W. Wei, *Int. J. Miner. Metall. Mater.* 20, 931 https://doi.org/10.1007/s12613-013-0817-1 (2013).
27. D. Degerman, M. Shipilin, P. Lömker, M. Soldemo, C. Goodwin, M. Wagstaffe, M. Börner, C. Schlueter, P. Amann, and A. Nilsson, *J. Phys. Chem. C* 128, 5542 https://doi.org/10.1021/acs.jpcc.3c08180 (2024).
28. J. Moulder, J. Chastain, and R. King, *Chem. Phys. Lett.* 220, 7 (1992).